Extension of the entropy viscosity method to the low Mach regime for the multi-D Euler equations (with variable area).

Marc O. Delchini[a], Jean C. Ragusa[*,a], Ray A. Berry[b]

[a] *Department of Nuclear Engineering, Texas A&M University, College Station, TX 77843, USA*
[b] *Idaho National Laboratory, Idaho Falls, ID 83415, USA*

Abstract

The entropy viscosity method, introduced by Guermond et al. [1, 2], is applied to the multi-D Euler equations with variable area for subsonic and supersonic flows. The entropy minimum principle is used to derive the dissipative terms for the mutli-D Euler equations with variable area on the model of [3]. It is also shown that the current definition of the viscosity coefficients ([1]) is unadpated to subsonic flow and thus requires a fix. A low Mach asymptotic study is performed to derive a new definition for the viscosity coefficients that are well-scaled in the low Mach regime. Multiple 1- and 2-D tests are run with the Ideal and Stiffened Gas equation of state: flow in a convergent-divergent nozzle, Leblanc shock tube, subsonic flow over a 2-D cylinder and circular hump, and supersonic flow in a compression corner. These tests allow to validate our new approach. Convergence studies are performed when an analytical solution is available for the 1-D case.

Key words: Euler equations with variable area, entropy viscosity method, stabilization method, low Mach regime, shocks.

1. Introduction

Over the past years an increasing interest raised for computational methods that can solve both compressible and incompressible flows. In engineering applications, there is often the need to solve for complex flows where a near incompressible regime or low Mach flow coexists with a supersonic flow domain. For example, such flow are encountered in aerodynamic in the study of airships. In the nuclear industry, flows are nearly the incompressible regime but compressible effects cannot be neglected because of the heat source and thus needs

*Corresponding author
Email addresses: delchmo@tamu.edu (Marc O. Delchini), jean.ragusa@tamu.edu (Jean C. Ragusa), ray.berry@inl.gov (Ray A. Berry)

to be accurately resolved.

When solving the multi-D Euler equations for a wide range of Mach numbers, multiple problems have to address: stability, accuracy and acceleration of the convergence in the low Mach regime. Because of the hyperbolic nature of the equations, shocks can form during transonic and supersonic flows, and require the use of the numerical methods in order to stabilize the scheme and correctly resolve the discontinuities. The literature offers a wide range of stabilization methods: flux-limiter [4, 5], pressure-based viscosity method ([6]), Lapidus method ([7, 8, 9]), and the entropy-viscosity method([1, 2]) among others. These numerical methods are usually developed using simple equation of states and tested for transonic and supersonic flows where the disparity between the acoustic waves and the fluid speed is not large since the Mach number is of order one. This approach leads to a well-known accuracy problem in the low Mach regime where the fluid velocity is smaller that the speed of sound by multiple order of magnitude. The numerical dissipative terms become ill-scaled in the low Mach regime and lead to the wrong numerical solution by changing the nature of the equations solved. This behavior is well documented in the literature [10, 11, 12] and often treated by performing a low Mach asymptotic study of the multi-D Euler equation. This method was originally used (REF) to show convergence of the compressible multi-D Euler equations to the incompressible ones. Thus, by using the same method, the effect of the dissipative terms in the low Mach regime, can be understood and, when needed, a fix is developed in order to ensure the convergence of the equations to the correct physical solution. This approach was used as a fixing method for multiple well known stabilization methods alike Roe scheme ([13]) and SUPG [12] while preserving the original stabilization properties of shocks.

We propose, through this paper, to investigate how the entropy viscosity method, when applied to the multi-D Euler equations with variable area, behaves in the low Mach regime. This method was initially introduced by Guermond et al. to solve for the hyperbolic systems and has shown good results when used for solving the multi-D Euler equations with various discretization schemes. More importantly, it is simple to implement, can be used with unstructured grids, and its dissipative terms are consistent with the entropy minimum principle and proven valid for any equation of state under certain conditions [3].

This paper is organized as follows: in Section 2 the current definition of the entropy viscosity method is recalled, and inconsistency with the low Mach regime are pointed out. Since our interest is in the variable area version of the multi-D Euler equation, the reader is guided trough the steps leading to the derivation of the dissipative terms on the model of [3]. Then in Section 3, a new definition of the viscosity coefficient is introduced and derived from a low Mach asymptotic study. After detailing the spatial and temporal discretization method in Section 4, 1- and 2-D numerical results are presented in Section 5 for a wide range of Mach numbers in order to validate the new : low Mach flow over a cylinder and a circular bump, and supersonic flow in a compression corner [14]. Convergence studied are performed in 1-D, in order to demonstrate the accuracy of the solution.

For purpose of clarity, the multi-D Euler equations with variable area are recalled in Eq. (1) and the corresponding variables are defined:

$$\begin{cases} \partial_t \left(\rho A\right) + \vec{\nabla}\cdot\left(\rho \vec{u} A\right) = 0 \\ \partial_t \left(\rho \vec{u} A\right) + \vec{\nabla}\cdot\left[\left(\rho \vec{u} \otimes \vec{u} + P\mathbf{I}\right) A\right] = P \vec{\nabla} A \\ \partial_t \left(\rho E A\right) + \vec{\nabla}\cdot\left[\vec{u}\left(\rho E + P\right) A\right] = 0 \\ P = P\left(\rho, e\right) \end{cases} \tag{1}$$

where ρ, $\rho\vec{u}$ and ρE are the density, the momentum and the total energy, respectively, and will be referred to as the conservative variables. The pressure P is computed with an equation of state expressed in function of the density ρ and the specific internal energy e. The tensor product $\vec{a} \otimes \vec{b}$ is taken with the following convention: $(\vec{a} \otimes \vec{b})_{i,j} = a_i b_j$. Lastly, the terms ∂_t, $\vec{\nabla}$, $\vec{\nabla}\cdot$ and $\mathbf{I}$ denote the temporal derivative, the gradient and divergent operators, and the identity tensor, respectively. The variable area A is assumed spatial dependent.

2. The Entropy Viscosity Method

2.1. Background

In this section, the entropy-based viscosity method [1, 2, 15] is recalled for the multi-D Euler equations (with constant area A) [16]. As mentioned in Section 1 the entropy-based viscosity method consists of adding dissipative terms, with a viscosity coefficient modulated by the entropy production which allows high-order accuracy when the solution is smooth. Thus, two questions arise: (i) how are the viscosity dissipative terms derived and (ii) how to numerically compute the entropy production. Answers to the first question can be found in [3] by Guermond et al., that details the proof leading to the derivation of the artificial dissipative terms (Eq. (2)) consistent with the entropy minimum principle theorem. The viscous regularization obtained is valid for any equation of state as long as the opposite of the physical entropy function, s, is convex with respect to the internal energy e and the specific volume $1/\rho$. As for the entropy production, it is locally evaluated by computing the local entropy residual $D_e(\vec{x}, t)$ defined in Eq. (4), that is peaked in shocks.

$$\begin{cases} \partial_t \left(\rho\right) + \vec{\nabla}\cdot\left(\rho \vec{u}\right) = \vec{\nabla}\cdot\left(\kappa \vec{\nabla} \rho\right) \\ \partial_t \left(\rho \vec{u}\right) + \vec{\nabla}\cdot\left(\rho \vec{u} \otimes \vec{u} + P\mathbf{I}\right) = \vec{\nabla}\cdot\left(\mu \rho \vec{\nabla}^s \vec{u} + \kappa \vec{u} \otimes \vec{\nabla} \rho\right) \\ \partial_t \left(\rho E\right) + \vec{\nabla}\cdot\left[\vec{u}\left(\rho E + P\right)\right] = \vec{\nabla}\cdot\left(\kappa \vec{\nabla}\left(\rho e\right) + \frac{1}{2}||\vec{u}||^2 \kappa \vec{\nabla} \rho + \rho \mu \vec{u} \vec{\nabla} \vec{u}\right) \\ P = P\left(\rho, e\right) \end{cases} \tag{2}$$

where κ and μ are local positive viscosity coefficients. $\vec{\nabla}^s \vec{u}$ denotes the symmetric gradient operator that guarantees the method to be rotational invariant [3].

In the current version of the method, κ and μ are set equal, so that the above viscous regularization (Eq. (2)) is equivalent to the parabolic regularization

[17] when considering the 1-D form of the equation. The current definition includes a first-order viscosity coefficient referred to with the subscript max, and a high-order viscosity coefficient referred to with the subscript e. The first-order viscosity coefficients μ_{max} and κ_{max} are proportional to the local largest eigenvalue $||\vec{u}|| + c$ and equivalent to an upwind-scheme (see Eq. (3)), when used, which is known to be over-dissipative and monotone [18]:

$$\mu_{max}(\vec{r}, t) = \kappa_{max}(\vec{r}, t) = \frac{h}{2} \left(||\vec{u}|| + c \right), \tag{3}$$

where h is defined as the ratio of the grid size to the polynomial order of the test functions used.
The second-order viscosity coefficients κ_e and μ_e are set proportional to the entropy production that is evaluated by computing the local entropy residual D_e. It also includes the interfacial jump of the entropy flux J that will allow to detect any discontinuities other than shocks:

$$\mu_e(\vec{r}, t) = \kappa_e(\vec{r}, t) = h^2 \frac{\max\left(|D_e(\vec{r}, t)|, J\right)}{||s - \bar{s}||_\infty} \text{ with } D_e(\vec{r}, t) = \partial_t s + \vec{u} \cdot \vec{\nabla} s \tag{4}$$

where $|| \cdot ||_\infty$ and $\bar{\cdot}$ denote the infinite norm operator and the average operator over the entire computational domain, respectively. The definition of the jump J is discretization-dependent and examples of definition can be found in [16] for DGFEM. The denominator $||s - \bar{s}||_\infty$ is used for dimensionality purposes and should not be of the same order as h, on penalty of loosing the high-order accuracy. Currently, there are no theoretical justification for choosing the denominator.
The definition of the viscosity coefficients μ and κ is function of the first- and second-order viscosity coefficients as follows:

$$\mu(\vec{r}, t) = \min\left(\mu_e(\vec{r}, t), \mu_{max}(\vec{r}, t)\right) \text{ and } \kappa(\vec{r}, t) = \min\left(\kappa_e(\vec{r}, t), \kappa_{max}(\vec{r}, t)\right). \tag{5}$$

This definition allows the following properties. In shock regions, the second-order viscosity coefficient experiences a peak because of entropy production, and thus, saturates to the first-order viscosity that is known to be over-dissipative and will smooth out oscillations. Anywhere else, the entropy production being small, the viscosity coefficients μ and κ are of order h^2.
Using the above definition of the entropy-based viscosity method, high-order accuracy was demonstrated and excellent results were obtained with 1-D Sod shock tubes and various 2-D tests [1, 2, 16].

2.2. Issues in the Low-Mach Regime

In the Low-Mach Regime, the flow is known to be isentropic resulting in very little entropy production. Since the entropy viscosity method is directly based on the evaluation of the local entropy production, it will be interested to study how the entropy viscosity coefficients μ and κ scale in the low Mach regime. Mathematically, it means that the entropy residual D_e will be very small, so will be the denominator $||s - \bar{s}||_\infty$, thus making the ratio, used in the definition of the viscosity coefficients Eq. (4), undetermined. Therefore, the current definition of the viscosity coefficients seems unadapted to subsonic flow and could lead to ill-scaled dissipative terms. A solution would be to recast the entropy residual as a function of other variables in order to have more freedom in the choice of the normalization parameter. With this approach, the viscosity coefficients are still defined proportional to the entropy residual that is a good indicator of the flow type (subsonic, transonic and supersonic flow). Plus, a different normalization parameter could be chosen, based on a low Mach asymptotic study so that the viscosity coefficients are well-scaled in the low Mach asymptotic limit (see Section 3).

2.3. The dissipative-terms for the multi-D Euler equations with variable area

One of the focus of this paper is to investigate the application of the entropy viscosity method to the multi-D Euler equations with variable area. The variable area version of the Euler equations is mostly used in 1-D and 2-D for obvious reasons, and differs from Eq. (1) by the momentum equation as shown in Eq. (6), that contains a non-conservative term proportional to the area gradient. For the purpose of this paper, the variable area is assumed to be a smooth function and only spatial dependent. An example can be found in [19] where a fluid flows through a 1-D convergent-divergent nozzle and reaches a steady-state solution.

$$\begin{cases} \partial_t \left(\rho A\right) + \vec{\nabla}\cdot\left(\rho \vec{u} A\right) = 0 \\ \partial_t \left(\rho \vec{u} A\right) + \vec{\nabla}\cdot\left[A\left(\rho \vec{u}\otimes\vec{u} + P\mathbf{I}\right)\right] = P\vec{\nabla}A \\ \partial_t\left(\rho E\right) + \vec{\nabla}\cdot\left[\vec{u}\left(\rho E + P\right)\right] = 0 \end{cases} \tag{6}$$

The application of the entropy viscosity method to the above system of equations is expected to be straightforward since it degenerates to the Eq. (1) when assuming a constant area. Details of the derivations of the dissipative terms are available to the reader in APPENDIX and are very similar to what was done in [3]: an entropy residual is derived without the dissipative terms. Then, the same entropy residual is re-derived after adding dissipative terms to each equation of the system given in Eq. (6), and the entropy minimum principle is used as a condition to obtain a definition for each of the dissipative terms. The final result including the dissipative terms is given in Eq. (7):

$$\begin{cases} \partial_t \left(\rho A\right) + \vec{\nabla}\cdot\left(\rho \vec{u} A\right) = \vec{\nabla}\cdot\left(A\kappa\vec{\nabla}\rho\right) \\ \partial_t \left(\rho \vec{u} A\right) + \vec{\nabla}\cdot\left[A\left(\rho \vec{u}\otimes\vec{u} + P\mathbf{I}\right)\right] = P\vec{\nabla}A + \vec{\nabla}\cdot\left[A\left(\mu\rho\vec{\nabla}^s\vec{u} + \kappa\vec{u}\otimes\vec{\nabla}\rho\right)\right] \\ \partial_t\left(\rho E\right) + \vec{\nabla}\cdot\left[\vec{u}\left(\rho E + P\right)\right] = \vec{\nabla}\cdot\left[A\left(\kappa\vec{\nabla}\left(\rho e\right) + \frac{1}{2}||\vec{u}||^2\kappa\vec{\nabla}\rho + \rho\mu\vec{u}\vec{\nabla}\vec{u}\right)\right] \end{cases} \tag{7}$$

The dissipative terms are very similar to the ones obtained for the multi-D Euler equations: each dissipative flux is multiplied by the variable area A in order to ensure conservation of the flux. When assuming a constant area, Eq. (2) is retrieved. The definition of the viscosity coefficients μ and κ is explained in Section 3.2.

3. All-speed Reformulation of the Entropy Viscosity Method

In this section, it is shown how the entropy residual D_e can be recast as a function of the pressure, the density and the speed of sound. Then, a low Mach asymptotic study of the multi-D Euler equations is performed in order to derive the correct normalization parameter.

3.1. New Entropy Production Residual

The first step in defining a viscosity coefficient that behaves well in the low mach limit is to recast the entropy residual in terms of the thermodynamic variables as shown in Eq. (8):

$$D_e(\vec{r},t) = \partial_t s + \vec{u}\cdot\vec{\nabla} s = \frac{s_e}{P_e}\left(\underbrace{\frac{dP}{dt} - c^2\frac{d\rho}{dt}}_{\tilde{D}_e(\vec{r},t)}\right), \tag{8}$$

where $\frac{d\cdot}{dt}$ denotes the material or total derivative, and P_e is the partial derivative of pressure with respect to internal energy. The steps that lead to the new formulation of the entropy residual D_e can be found in APPENDIX.
The entropy residual D_e and $\tilde{D}_e$ are proportional to each other and therefore will experience the same variation when taking the absolute value. Thus, locally evaluating $\tilde{D}_e$ instead of D_e should allow us to measure the entropy production point wise. This new expression given in Eq. (8) has multiple advantages:

- an analytical expression of the entropy function is not longer needed: the entropy residual $\tilde{D}_e$ is evaluated using the local values of the pressure, the density and the speed of sound. Deriving an entropy function for some complex equation of states can be difficult.

- with the proposed expression of the entropy residual function of pressure and density, additional normalizations suitable for low Mach flows of the entropy residual can be devised. Examples include the pressure itself, or combination of the density, the speed of sound and the norm of the velocity: ρc^2, $\rho c||\vec{u}||$ and $\rho||\vec{u}||^2$.

The viscosity coefficients μ and κ are now defined proportional to the new entropy residual $\tilde{D}_e$ on the model of Eq. (4) as follows:

$$\mu\left(\vec(r),t\right) = \kappa\left(\vec(r),t\right) = h^2\frac{\max\left(\tilde{D}_e, J\right)}{n(P)} \tag{9}$$

where $n(P)$ is a normalization parameter to determine and all other variables were defined previously.
As mentioned earlier, the normalization parameter $n(P)$ must be of the same units as the pressure for the viscosity coefficients to have the unit of a dynamic viscosity (m^2/s). Multiples options are available to us (P, ρc^2, $\rho c||\vec{u}||$

and $\rho||\vec{u}||^2$). The choice of the normalization parameter cannot be random if the definition of the viscosity coefficient is wanted to be well-scaled for a wide range of Mach numbers. For example, by choosing $n(P) = \rho||\vec{u}||^2$, the viscosity coefficient will become very large as the Mach number decreases which would be unnecessary since the equations will not develop any shock or discontinuity. Therefore, it is proposed to carry, in Section 3.2, a low-Mach asymptotic study of the multi-D Euler equations in order to determine the correct expression for the normalization parameter $n(P)$.

3.2. Low-Mach asymptotic study of the multi-D Euler equations

The asymptotic study requires the multi-D Euler equations to be non dimensionalized: the objective is to make the Mach number appears and thus, use a polynomial expansion of the variables as a function of the Mach number in order to derive the leading, first- and second-order equations. Before detailing the steps of the asymptotic method, let us have a closer look at the system of equations under consideration. The initial system of equations is composed of the multi-D Euler equations. For stability purpose, artificial dissipative terms are added to each equation as explained in Section 2. The resulting system of equations is alike the multi-D Navier-Stokes equations in a sense that it contains second-order derivative terms. Thus, it would be interesting to look at the steps employed in the asymptotic study of the multi-D Navier-Stokes equations in order to understand how the dissipative terms are treated. Fortunately, this process is well-documented in the literature [10, 11, 12] for both multi-D Euler equations and Navier-Stokes equations. The work presented here is mainly inspired of [20] that focuses on the asymptotic study in the low Mach regime of Navier-Stokes equations. During the derivation, the reader has to keep in mind that the objective of this section is to derive a normalization parameter for the definition of the viscosity coefficients so that the multi-D Euler equations degenerate to the incompressible system of equations, which implies that the dissipative terms are well-scaled. The full derivation that leads to the final result can be found in APPENDIX. In this section, only the main steps are recalled.

To express Eq. (2) in dimensionless variables, the following definitions are used

$$\begin{aligned} \rho &= \frac{\rho^*}{\rho_\infty}, \, P = \frac{P^*}{\rho_\infty c_\infty^2}, \, \mu = \frac{\mu^*}{\mu_\infty}, \, , \, E = \frac{E^*}{c_\infty^2}, \, \mu = \frac{\mu^*}{\mu_\infty}, \\ \kappa &= \frac{\kappa^*}{\kappa_\infty}, \, x = \frac{x^*}{L_\infty}, \, t = \frac{t^*}{L_\infty / u_\infty}, \, u = \frac{u^*}{u_\infty} \end{aligned} \tag{10}$$

where the subscript ∞ and the upper script $*$ denote far field or stagnation quantities and the dimensionless variables, respectively. The reference quantities are chosen such that the non dimensional flow quantities are of order one for any low reference-Mach number

$$M_\infty = \frac{u_\infty^*}{c*_\infty} \tag{11}$$

where c^*_∞ is a reference value for the speed of sound. Then, using the non dimensional quantities and the multi-D Euler equations from Eq. (2) , the following non dimensional form is obtained:

$$\begin{cases} \partial_t \rho + \nabla \left(\rho \vec{u}\right) = \frac{1}{Re_\infty Pr_\infty} \nabla \cdot \left(\kappa \nabla \rho\right) \\ \partial_t \left(\rho \vec{u}\right) + \nabla \left(\rho \vec{u} \otimes \vec{u}\right) + \frac{1}{M_\infty^2} \nabla \left(P\right) = \frac{1}{Re_\infty} \nabla \left(\rho \mu \nabla \vec{u}\right) + \frac{1}{Re_\infty Pr_\infty} \nabla \cdot \left(\vec{u} \otimes \kappa \nabla \rho\right) \\ \partial_t \left(\rho E\right) + \nabla \cdot \left[\vec{u} \left(\rho E + P\right)\right] = \frac{1}{Re_\infty Pr_\infty} \nabla \cdot \left(\kappa \nabla (\rho e)\right) + \frac{\tilde{M_\infty}^2}{Re_\infty} \nabla \cdot \left(\vec{u} \rho \mu \nabla \vec{u}\right) \\ + \frac{M_\infty^2}{2 Re_\infty Pr_\infty} \nabla \cdot \left(\kappa u^2 \nabla \rho\right) \\ P = \left(\gamma - 1\right) \left(\rho E + M_\infty^2 \rho u^2\right) \end{cases}$$

where the *numerical* Reynolds (Re_∞) and Prandtl (Pr_∞) numbers are defined as follows:

$$Re_\infty = \frac{u_\infty L_\infty}{\mu_\infty} \text{ and } Pr_\infty = \frac{\mu_\infty}{\kappa_\infty}. \tag{12}$$

Since it is chosen to have the same definition for both μ and κ the numerical Prandtl number is unconditionally equal to one: $Pr_\infty = 1$.
Once the dimensionless equations are obtained, the next step consists of expanding each variable in term of the Mach number (example given in Eq. (13) for the pressure P) in order to derive the leading, first- and second-order equations.

$$P(\vec{r}, t) = P_0(\vec{r}, t) + P_1(\vec{r}, t) M_\infty + P_2(\vec{r}, t) M_\infty^2 + \ldots \text{ with } M_\infty \to 0 \tag{13}$$

Before deriving the leading-order equation, a choice needs to be made on how the numerical Reynolds number scales. Multiple options are available to us and a few example are given: $Re_\infty = M_\infty$, or $Re_\infty = M_\infty^{-1}$ or $Re_\infty = 1$. Let us assume for academy purpose that the numerical Reynolds number scales as the inverse of the Mach number square: $Re_\infty = M_\infty^{-2}$. The best way to evaluate the impact of this choice on the equations, is to look at the momentum equation and try to derive the order M_∞^{-2}:

$$\vec{\nabla} P_0 = \vec{\nabla} \cdot \left(\rho_0 \mu_0 \vec{\nabla} \vec{u}_0 + \vec{u}_0 \otimes \vec{\nabla} \rho_0\right) \tag{14}$$

which is known to be ([12])

$$\vec{\nabla} P_0 = 0 \tag{15}$$

It is clear that Eq. (14) and Eq. (15) will not yield the same result. The same conclusion is drawn when deriving the order M_∞^{-1} of the momentum equation, making our initial assumption not suitable. From the above result, it is understood that the numerical Reynolds number has to scale as one so that it does not affect the orders M_∞^{-2} and M_∞^{-1} of the momentum equations: $Re_\infty = 1$.

Thus, with such assumption, Eq. (12) implies:

$$
\begin{aligned}
&\text{At order } M_\infty^{-2}: \\
&\vec{\nabla} P_0 = 0 \\
&\text{At order } M_\infty^{-1}: \\
&\vec{\nabla} P_1 = 0 \\
&\text{At leading-order:} \\
&\partial_t \rho_0 + \vec{\nabla}\cdot(\rho_0 \vec{u}_0) = \vec{\nabla}\cdot(\kappa_0 \vec{\nabla}\rho_0) \\
&\partial_t(\rho_0 \vec{u}_0) + \vec{\nabla}\cdot(\rho_0 \vec{u}_0 \otimes \vec{u}_0) + \vec{\nabla} P_2 = \vec{\nabla}\cdot(\rho_0 \mu_0 \vec{\nabla}\vec{u}_0 + \vec{u}_0 \otimes \vec{\nabla}\rho_0) \\
&\partial_t(\rho_0 E_0) + \vec{\nabla}\cdot[\vec{u}_0(\rho_0 E_0 + P_0)] = \vec{\nabla}\cdot(\kappa_0 \vec{\nabla}(\rho_0 e_0))
\end{aligned}
$$

Under this form, the dissipative terms are well-scaled and should not alter the physical solution in the asymptotic limit.

It is now determined that the numerical Reynolds number Re_∞ has to scale as one. Following Eq. (12), Re_∞ is a function of the μ_∞, and thus n_P. It can be shown using Eq. (10) and the definitions of $\tilde{D}$ given in Eq. (8) that:

$$\mu_\infty = \frac{\rho_\infty c_\infty^2 u_\infty L}{n_{P,\infty}} \tag{16}$$

where $n_{P,\infty}$ is the far-field quantity for the normalization parameter n_P. Substituing Eq. (16) into Eq. (12) and remembering that the numerical Reynolds number scales as one, it yields:

$$n_{P,\infty} = \rho_\infty c_\infty^2 \tag{17}$$

Eq. (17) tells us that in the asymptotic limit, the normalization parameter n_P scales as $\rho_\infty c_\infty^2$ which leaves us with two options: either $n_P = \rho c^2$ or $n_P = P$. The choice was made to use $n_P = \rho c^2$ in the asymptotic limit (it was found to behave well as shown in Section 5) which ,we believe, is more representative of the flow type. This definition is only valid in the asymptotic limit and the purpose of this paper is to define a viscosity coefficient μ that is valid for a wide range of Mach numbers. Thus, it is proposed to define the high-order viscosity coefficient μ_e as follows:

$$\mu_e = h^2 \frac{\max(\tilde{D}_e, J)}{(1 - f(M))\rho c^2 + f(M)\rho ||\vec{u}||^2} \tag{18}$$

where $f(M)$ is a function of the local Mach number M with the following properties:

$$\begin{cases} f(M) \to 0 \text{ as } M \to 0 \\ f(M) \to 1 \text{ as } M \geq 1 \end{cases} \tag{19}$$

The choice of the function $f(M)$ is not fixed and a few examples are available in the literature. (REF) proposed the simple definition $f(M) = \min(M, 1)$ which meets the conditions of Eq. (19). Another definition for $f(M)$ was proposed by [13]:

$$f(M) = \tag{20}$$

All of the numerical results presented in Section 5 were obtained by using $f(M) = \min(M, 1)$ which is simple to implement. A convergence test for a subsonic flow over a 2-D cylinder will show that this definition of $f(M)$ yields the correct behavior in the asymptotic limit. The definition of the high-order viscosity coefficient $\mu_e(\vec{r}, t)$ should behave well for complex flow where a near incompressible regime coexists with a supersonic flow domain since $f(M)$ is function of the local Mach number.
For clarity purpose, the full definition of the viscosity coefficient $\mu(\vec{r}, t)$ is recalled:

$$\begin{cases} \mu(\vec{r}, t) = \max(\mu_{max}(\vec{r}, t), \mu_e(\vec{r}, t)) \\ \text{where } \mu_{max}(\vec{r}, t) = \frac{h}{2}(||\vec{u}|| + c) \\ \text{and } \mu_e(\vec{r}, t) = h^2 \frac{\max(\tilde{D}_e, J)}{(1-f(M))\rho c^2 + f(M)\rho ||\vec{u}||^2} \\ \mu(\vec{r}, t) = \kappa(\vec{r}, t) \end{cases} \tag{21}$$

These viscosity coefficients are valid for both the multi-D Euler equations with variable and constant area and are employed with the dissipative terms detailed in Eq. (12). The reader will notice that, through the derivation, none assumption was made on the type of equation of state besides the convexity condition on the entropy function s. The remaining of this paper (Section 5) will focus on demonstrating that the definition of the viscosity coefficient given in Eq. (21) is indeed well-scaled in the asymptotic limit and that shocks are still well resolved.

4. Solution Techniques Spatial and Temporal Discretizations

In order to detail the partial and temporal discretization used for this study, the system of equations Eq. (7) is considered under the following form for simplicity:

$$\partial_t U + \vec{\nabla} \cdot F\left(U\right) = S \tag{22}$$

where U is the vector solution, F is a conservative vector flux and S is a vector source that can contain some relaxation source terms and non-conservative terms.

4.1. Spatial and Temporal Discretizations

The system of equation given in Eq. (22) is discretized using a continuous Galerkin finite element method and high-order temporal integrators provided by the MOOSE framework.

4.1.1. CFEM

In order to apply the continuous finite element method, Eq. (22) is multiplied by a smooth test function ϕ, integrated by part and each integral is split onto each finite element e of the discrete mesh Ω bounded by $\partial\Omega$, to obtain a weak solution:

$$\sum_e \int_e \partial_t U \phi - \sum_e \int_e F(U) \cdot \vec{\nabla}\phi + \int_{\partial\Omega} F(U)\vec{n}\phi - \sum_e \int_e S\phi = 0 \qquad (23)$$

The integrals over the elements e are evaluated using quadrature-point rules. The Moose framework provides a wide range of test function and quadrature rules: trapezoidal and Gauss rules among others. Linear Lagrange polynomials will be used as test functions and should ensure second-order convergence for smooth functions. The order of convergence will be demonstrated.

4.1.2. Temporal integrator

The MOOSE framework offers both first- and second-order explicit and implicit temporal integrators. In all of the numerical examples presented in Section 5, the time-dependent term $\int_e \partial_t U \phi$ will be evaluated using the second-order temporal integrator BDF2. By considering three converged solutions, U^{n-1}, U^n and U^{n+1} at three different time t^{n-1}, t^n and t^{n+1}, respectively, it yields:

$$\begin{aligned}
\int_e \partial_t U \phi &= \int_e \left(\omega_0 U^{n+1} + \omega_1 U^n + \omega_2 U^{n-1}\right)\phi \qquad (24)\\
\text{with } \omega_0 &= \frac{2\Delta t^{n+1} + \Delta t^n}{\Delta t^{n+1}\left(\Delta t^{n+1} + \Delta t^n\right)},\\
\omega_1 &= -\frac{\Delta t^{n+1} + \Delta t^n}{\Delta t^{n+1}\Delta t^n}\\
\text{and } \omega_2 &= \frac{\Delta t^{n+1}}{\Delta t^n\left(\Delta t^{n+1} + \Delta t^n\right)}
\end{aligned}$$

where $\Delta t^n = t^n - t^{n-1}$ and $\Delta t^{n+1} = t^{n+1} - t^n$.

4.2. Boundary conditions

The boundary conditions will be treated by either using Dirichlet or Neumann conditions. The multi-D Euler equations are wave-dominated systems that require great care when dealing with boundary conditions. It is often recommended to use the characteristic equations to compute the correct flux at the boundaries. Our implementation of the boundary conditions will follow the method described in [19] that was developed for Ideal Gas and Stiffened Gas equation of states. For each numerical solution presented in Section 5, the type of boundary conditions used will be specified: supersonic inlet, subsonic inlet (stagnation pressure boundary), supersonic outlet and subsonic inlet (static pressure boundary).

4.3. Solver

A Free-Jacobian-Newton-Krylov (FJNK) method is used to solve for the solution at each time step. The jacobian matrix of the discretized equations was derived by hand, hard coded and used as a preconditioner. This method requires the partial derivative of the pressure with respect to the conservative variables to be known. The contribution of the artificial dissipative terms to the jacobian matrix is simplified by assuming constant viscosity coefficients as shown in Eq. (25) for the dissipative terms of the continuity equation:

$$\frac{\partial}{\partial U_i}\left(\kappa \vec{\nabla}\rho\vec{\nabla}\phi\right) = \kappa \frac{\partial}{\partial U_i}\left(\rho\right)\vec{\nabla}\phi \tag{25}$$

where U_i denotes the set of conservative variables.

5. Numerical Results

This section is dedicated to presenting 1- and 2-D numerical results obtained by solving Eq. (7) with the entropy viscosity method. This section has two objectives: validate our new definition of the viscosity coefficients for the low Mach limit, and, make sure that the new definition can still resolve shocks.

The first set of 1-D simulations consist of liquid water and steam flowing in a convergent-divergent nozzle. This test is interesting for multiple reasons: a steady-state is reached (some stabilization methods are known to have difficulties to reach a steady-state ([4, 5]), it can be performed for liquid and gas phases, and, an analytical solution of the steady-state solution is available which allow for convergence study. The 1-D Leblanc shock tube test [21] (in a straight pipe) is also performed and consists of a flow developing shocks. A convergence study will be performed in order to demonstrate convergence of the numerical solution to the exact solution.

This section also included 2-D simulations from subsonic to supersonic flows. Subsonic flows of a gas over a 2-D cylinder and a hump [22] are simulated and results are shown for various far-field Mach numbers. Numerical results of a supersonic flow in a compression corner are provided to illustrate the capabilities of the new definition in the supersonic case. Convergence studies are performed when an analytical solution is available.

For each simulation, informations relative to the boundary conditions and the equation of state will be provided. All of the numerical solution presented in this section are run with the second-order temporal integrator $BDF2$ and linear polynomials test functions. The integrals are numerically computed using a second-order Gauss quadrature rule.

The numerical results presented in Section 5 are all run using either the Ideal Gas [23] or Stiffened Gas equation of state [24]. A generic formulation is recalled in Eq. (26).

$$P = (\gamma - 1)\rho(e - q) - \gamma P_\infty \tag{26}$$

where the parameters q and P_∞ are fluid dependent and will be specified in time. Eq. (26) degenerates to the Ideal Gas equation of state by setting q and P_∞ to zero. The Ideal and Stiffened Gas equation of states have a convex entropy s:

$$s = C_v \ln\left(\frac{P + P_\infty}{\rho^{\gamma-1}}\right)$$

5.1. Liquid water in a 1-D divergent-convergent nozzle

The simulation consists of liquid water flowing through a 1-D convergent-divergent nozzle with the following equation, $A(x) = 1 + 0.5\cos(2\pi x/L)$, where $L = 1m$ is the length of the nozzle. At the inlet, the stagnation pressure and temperature are set to $P_0 = 1MPa$ and $T_0 = 453K$, respectively. At the outlet, only the static pressure is specified: $P_s = 0.5MPa$. Details about the theory related to the inlet and outlet boundary conditions can be found in (REFS). Initially, the temperature is uniform and set equal to the stagnation temperature and the pressure linearly decreases from the stagnation pressure to the static one. Finally, the liquid is assumed at rest. The Stiffened Gas equation of state is used to model the liquid water with the parameters provided in Table 1.

Table 1: Stiffened Gas Equation of State parameters for liquid water.

γ	$C_v\ (J \cdot kg^{-1} \cdot K^{-1})$	$P_\infty\ (Pa)$	$q\ (J \cdot kg^{-1})$
2.35	1816	10^9	-1167.10^3

Because of the low pressure difference between the inlet and the outlet, and the large value of P_∞, the flow remains subsonic and thus, should not display any shock. Enthalpy and entropy are conserved through the nozzle, and these conservation relations are used to determine the exact solution at steady-state (REF). Plots of the velocity, density and pressure are given at steady-state in Fig. 1a, Fig. 1b, Fig. 1c, respectively, along with the exact solution for comparison. The viscosity coefficients are also plotted in Fig. 1d. The mesh used is uniform and has 50 cells.

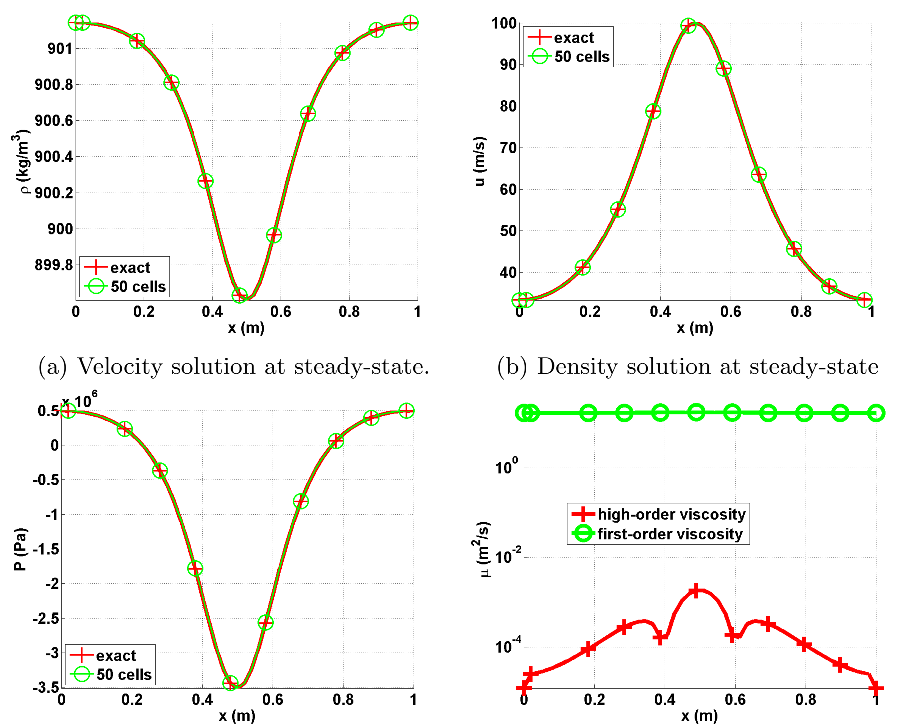

(a) Velocity solution at steady-state. (b) Density solution at steady-state

(c) Pressure solution at steady-state. (d) Viscosity coefficients at steady-state.

Figure 1: Steady-state solution for liquid phase in a 1-D convergent-divergent nozzle with an uniform mesh of 50 cells.

The numerical and exact solutions of the velocity, pressure and density given in Fig. 1 for a fairly coarse mesh (50 cells) perfectly overlap: it is noted that the numerical solution is symmetric with respect to the nozzle throat located in $x = 0.5m$. The second-order viscosity coefficient is very small compare to the first-order one as expected: (i) the numerical solution is smooth as shown in Fig. 1d and (ii) the flow is in a low Mach regime and thus isentropic . A convergence study was performed using the exact solution as a reference: the L1 and L2 norms of the error and the corresponding convergence rates are computed at steady-state on various uniform mesh from 4 to 256 cells. The results for linear polynomials $\mathbb{Q}_1$ are reported in Table 2 and Table 3 for the primitive variables: density, velocity and pressure.

Table 2: L1 norm of the error for the liquid phase in a 1-D convergent-divergent nozzle at steady-state.

cells	density	rate	pressure	rate	velocity	rate
4	$2.8037\ 10^{-1}$	–	$8.4705e\ 10^{5}$	–	7.2737	–
8	$1.3343\ 10^{-1}$	1.0713	$4.7893e\ 10^{5}$	0.24227	6.1493	0.074683
16	$2.9373\ 10^{-2}$	2.1835	$1.0613e\ 10^{5}$	2.3247	1.2275	2.4501
32	$5.1120\ 10^{-3}$	2.5225	$1.8446\ 10^{4}$	2.6959	$1.8943\ 10^{-1}$	3.0966
64	$1.0558\ 10^{-3}$	2.2755	$3.7938\ 10^{3}$	2.3207	$3.7919\ 10^{-2}$	2.3323
128	$2.3712\ 10^{-4}$	2.1547	$8.4471\ 10^{2}$	2.0624	$8.5517\ 10^{-3}$	2.0473
256	$5.6058\ 10^{-5}$	2.0806	$1.9839\ 10^{2}$	2.0478	$2.0475\ 10^{-3}$	1.9833
512	$1.3278\ 10^{-5}$	2.0778	46.622	2.0478	$4.9516\ 10^{-4}$	1.9669

Table 3: L2 norm of the error for the liquid phase in a 1-D convergent-divergent nozzle at steady-state.

cells	density	rate	pressure	rate	velocity	rate
4	$3.106397\ 10^{-1}$	–	$5.254445\ 10^{5}$	–	3.288543	–
8	$7.491623\ 10^{-2}$	2.07	$1.636966\ 10^{5}$	1.60	1.823880	0.90
16	$2.079858\ 10^{-2}$	1.80	$4.627338\ 10^{4}$	1.75	$4.990605\ 10^{-1}$	1.83
32	$5.329627\ 10^{-3}$	1.90	$1.180287\ 10^{4}$	1.92	$1.261018\ 10^{-1}$	1.93
64	$1.341583\ 10^{-3}$	1.94	$2.967104\ 10^{3}$	1.98	$3.160914\ 10^{-2}$	1.99
128	$3.359766\ 10^{-4}$	1.99	$7.428087\ 10^{2}$	1.99	$7.907499\ 10^{-3}$	1.99
256	$8.403859\ 10^{-5}$	1.99	$1.857861\ 10^{2}$	1.99	$1.977292\ 10^{-3}$	1.99
512	$2.10075\ 10^{-5}$	1.99	27.048	1.99	$4.9516\ 10^{-4}$	1.99

It is observed that the convergence rate for the L1 and L2 norm of the error is 2: the entropy viscosity method conserves the high-order accuracy when the numerical solution is smooth, and the new definition of the entropy viscosity coefficient seems to behave as expected in the low Mach limit.

5.2. Steam in a 1-D divergent-convergent nozzle

Instead of liquid water, we now simulate a flow of steam using the exact same 1-D geometry, initial conditions and boundary conditions as in Section 5.1. The Stiffened gas equation of state is still used but with different parameters that are given in Table 4: steam is a gas and compressible effects will become dominant.

Table 4: Stiffened Gas Equation of State parameters for steam.

γ	$C_v\ (J \cdot kg^{-1} \cdot K^{-1})$	$P_\infty\ (Pa)$	$q\ (J \cdot kg^{-1})$
1.43	1040	0	2030.10^{3}

The pressure difference applied between the inlet and outlet is large enough to make the steam accelerates through the nozzle and result in the formation of shock in the divergent part. The behavior is different from what is observed for the liquid water phase in Section 5.1 because of the liquid to gas density ratio that is of 1000. Even though a shock forms, an exact solution at steady-state is still available (REF). The objective of this section is to show that using the new definition of the viscosity coefficient in Eq. (21), the shock can be correctly resolved without spurious oscillation. The steady-state numerical solution is shown in Fig. 2 and was run with a mesh of 1600 cells.

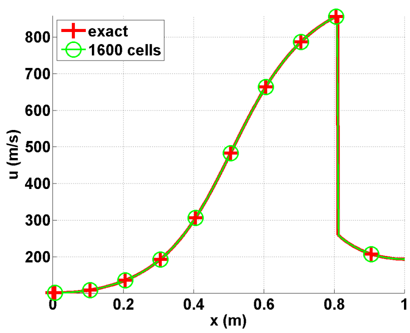

(a) Velocity solution at steady-state.

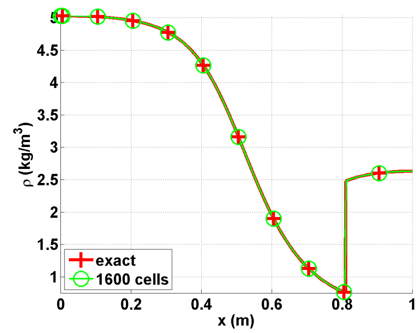

(b) Density solution at steady-state

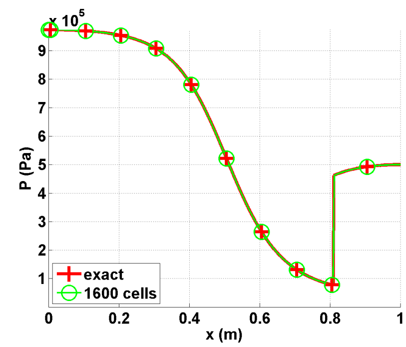

(c) Pressure solution at steady-state.

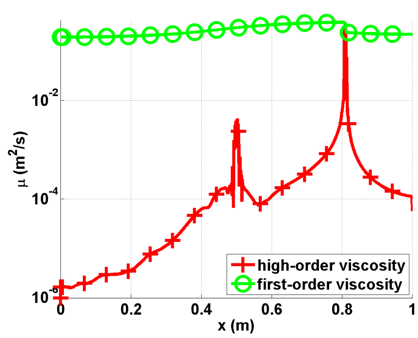

(d) Viscosity coefficients at steady-state.

Figure 2: Steady-state solution for vapor phase in a 1-D convergent-divergent nozzle.

The steady-state solution of the density, velocity and pressure are given in Fig. 2a, Fig. 2b and Fig. 2c. The steady-solution displays a shock around $x = 0.8m$ and match the exact solution. In Fig. 2d, the first- and second-order viscosity coefficients are log plotted at steady-state: the second-order viscosity coefficient is peaked in the shock region around $x = 0.8m$ as expected, and saturate to the first-order viscosity coefficient. The profile also displays another peak at $x = 0.5m$ that corresponds to the position of the sonic point for a 1-

D convergent-divergent nozzle: this particular point is known to develop small instabilities that are detected when computing the jumps of the pressure and density gradients. Anywhere else, the second-order viscosity coefficient is small. In order to prove convergence of the numerical solution to the exact solution, a convergence study is performed. Because of the presence of a shock, second-order accuracy cannot be achieved. However, the convergence rate is known and expected to be of 1 and 1/2 when computing the L1 and L2 norms of the error, respectively. Results are reported in Table 5 and Table 6 for the primitive variables: density, velocity and pressure.

Table 5: L1 norm of the error for the vapor phase in a 1-D convergent-divergent nozzle at steady-state.

cells	density	rate	pressure	rate	velocity	rate
5	$0.72562\ 10^{-1}$	–	$1.5657\ 10^{5}$	–	173.69	–
10	$0.4165\ 10^{-1}$	0.80088	$9.6741\ 10^{4}$	0.63425	120.69	0.52519
20	$0.20675\ 10^{-1}$	1.0104	$4.9193\ 10^{4}$	0.96971	72.149	0.74228
40	$0.093703\ 10^{-1}$	1.1417	$2.0103\ 10^{4}$	0.72728	34.716	1.0554
80	$0.047328\ 10^{-1}$	0.9854	$1.0208\ 10^{4}$	0.9777	16.082	1.1101
160	$0.023965\ 10^{-2}$	0.9817	$5.1969\ 10^{3}$	0.9739	7.9573	1.0150
320	$0.020768\ 10^{-2}$	0.9886	$2.5116\ 10^{3}$	1.0490	3.7812	1.0734
640	$0.0059715\ 10^{-2}$	1.0160	$1.2754\ 10^{3}$	0.9776	1.8353	1.0428

Table 6: L2 norm of the error for the vapor phase in a 1-D convergent-divergent nozzle at steady-state.

cells	density	rate	pressure	rate	velocity	rate
5	$9.7144\ 10^{-1}$	–	$2.0215\ 10^{5}$	–	236.94	–
10	$5.9718\ 10^{-1}$	0.70195	$1.3024\ 10^{5}$	0.63425	166.56	0.50854
20	$2.9503\ 10^{-1}$	1.0173	$6.6503\ 10^{4}$	0.96971	103.36	0.68831
40	$1.8193\ 10^{-1}$	0.69747	$4.0171\ 10^{4}$	0.72728	66.374	0.6390
80	$1.3366\ 10^{-1}$	0.44485	$2.3163\ 10^{4}$	0.43576	42.981	0.62692
160	$9.6638\ 10^{-2}$	0.46790	$1.7263\ 10^{4}$	0.42413	31.717	0.43844
320	$7.0896\ 10^{-2}$	0.44688	$1.2763\ 10^{4}$	0.43571	23.138	0.45499
640	$5.2191\ 10^{-2}$	0.44190	$9.4217\ 10^{3}$	0.43790	16.910	0.45238

The convergence rates for the L1 and L2 norms of the error are close to the theoretical values which prove convergence of the numerical solution to the exact solution.
It is also interesting to investigate the effect of the first-order viscosity onto the steady-state solution. In Fig. 3, the steady-state velocity profile is plotted when using the first- and second-order viscosity coefficients: the main difference between the two numerical solution is in the resolution of the shock around

$x = 0.8m$. The first-order viscosity coefficient is by definition more dissipative and will smooth out the solution. In the other hand, the high-order viscosity better resolves the shock and allow high-order accuracy away from the shock region. It is also noted that the numerical solution obtained with the first-order viscosity coefficient is satisfying: this is due to the nature of the solution that contains a standing shock, and thus, will force the shock to form even with large artificial dissipation.

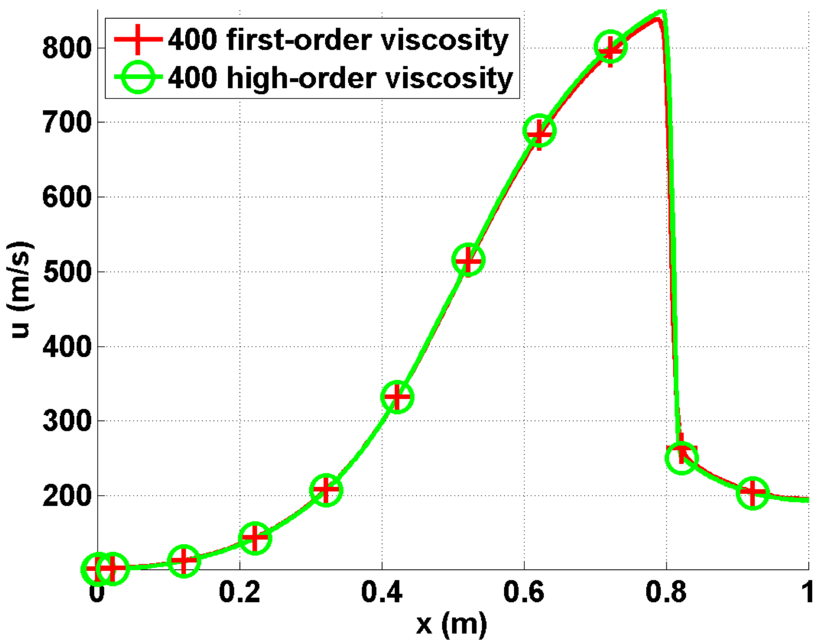

Figure 3: Velocity profile at steady-state with the first- and second-order viscosity for a mesh with 400 cells.

5.3. Leblanc shock tube

The 1-D Leblanc shock tube is a Riemann problem and designed to test the robustness and the accuracy of the stabilization method. The initial conditions are given in Table 7. The ideal gas equation of state is used to compute the fluid pressure with the following heat capacity ratio $\gamma = 5/3$.

Table 7: Initial conditions for the 1-D Leblanc shock tube.

	ρ	u	e
left	1.	0.	0.1
right	10^{-3}	0.	10^{-7}

This test is computationally challenging because of the large left to right pressure ratio. The computational domain consists of a 1-D pipe of length $L = 9m$ with an interface located at $x = 2m$. At $t = 0.s$, the interface is removed, allowing the fluid to move. The numerical solution is run until $t = 4.s$ and the density, momentum and total energy profiles are given in Fig. 4a, Fig. 4b and Fig. 4c, respectively, along with the exact solution. The viscosity coefficients are also plotted in Fig. 4d. These plots were run with three different uniform mesh of 800, 3200 and 6000 cells and a constant time step $\Delta t = 10^{-3}s.$.

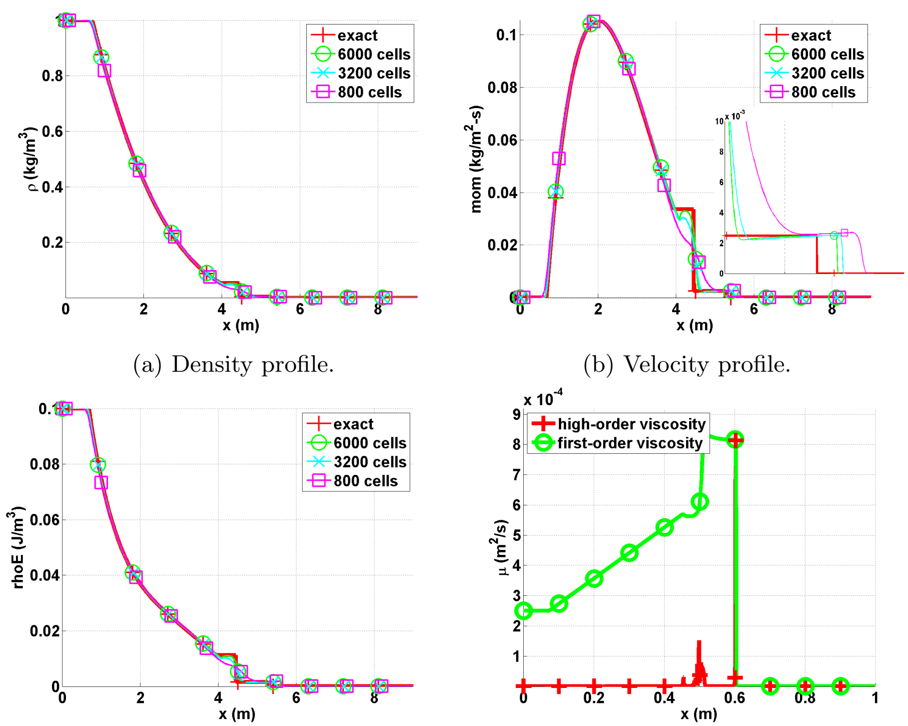

(a) Density profile.

(b) Velocity profile.

(c) Pressure profile.

(d) Viscosity coefficients.

Figure 4: Numerical solution for the 1-D Leblanc shock tube at $t = 4.s$.

The density, momentum and total energy profiles given in Fig. 4 do not display any oscillations. In Fig. 4b, the shock region is zoomed in for better resolution: the shock is well resolved and do not show any oscillation. It is also observed that the shock position of the numerical solution converges to the exact position when refining the mesh. The contact wave is shown in Fig. 4b at $x = 4.5m$. The second-order viscosity coefficient profile is shown in Fig. 4d and behaves as expected: it saturates to the first-order viscosity in the shock region and thus prevent oscillations from forming. In the contact wave at $x = 4.5m$, a smaller peak is observed that is due to the presence of the jumps in the definition of the second-order viscosity coefficient (Eq. (21)).

Once again, a convergence study is performed in order to prove convergence of the numerical solution to the exact solution. As for the vapor phase in the 1-D nozzle (Section 5.2), the expected convergence rate for the L1 and L2 norms of the error are 1 and 1/2, respectively. The exact solution was obtained by running a 1-D Riemann solver and used as a reference solution to compute the L1 and L2-norms of the error that are reported in Table 8 and Table 9 for the conservative variables: density, momentum and total energy.

Table 8: L1 norm of the error for the 1-D Leblanc test at $t = 4.s$.

cells	density	rate	momentum	rate
100	$1.0354722\ 10^{-2}$	–	$3.5471714\ 10^{-3}$	–
200	$7.2680512\ 10^{-3}$	0.51064841	$2.5933119\ 10^{-3}$	0.45187331
400	$5.0825628\ 10^{-3}$	0.51601245	$2.0668092\ 10^{-3}$	0.32739054
800	$3.4025056\ 10^{-3}$	0.57895861	$1.4793838\ 10^{-3}$	0.48240884
1600	$2.1649953\ 10^{-3}$	0.65223363	$9.7152832\ 10^{-4}$	0.6066684
3200	$1.2465433\ 10^{-3}$	0.79643094	$5.5937409\ 10^{-4}$	0.79644263
6400	$6.4476928\ 10^{-4}$	0.95107804	$3.0244198\ 10^{-4}$	0.88715502
12800	$3.3950948\ 10^{-4}$	0.92533116	$1.5958118\ 10^{-4}$	0.9223679

cells	total energy	rate
100	0.0014033046	–
200	$9.8611746\ 10^{-4}$	0.5089968
400	$7.7844421\ 10^{-4}$	0.34116585
800	$5.5702549\ 10^{-4}$	0.48285029
1600	$3.5720171\ 10^{-4}$	0.64100438
3200	$2.0491799\ 10^{-4}$	0.80169235
6400	$1.0914891\ 10^{-4}$	0.90874889
12800	$5.7909794\ 10^{-5}$	0.91441847

Table 9: L2 norm of the error for the 1-D Leblanc test at $t = 4.s$.

cells	density	rate	momentum	rate
100	$5.7187851\ 10^{-3}$	–	$1.7767236\ 10^{-3}$	–
200	$3.8995238\ 10^{-3}$	0.55241073	$1.4913161\ 10^{-3}$	0.25263314
400	$2.8103526\ 10^{-3}$	0.4725468	$1.3305301\ 10^{-3}$	0.164585
800	$2.1081933\ 10^{-3}$	0.41474398	$1.1398931\ 10^{-3}$	0.22310254
1600	$1.5731052\ 10^{-3}$	0.42239201	$9.0394227\ 10^{-4}$	0.33459602
3200	$1.0610667\ 10^{-3}$	0.56809979	$6.2735595\ 10^{-4}$	0.52694639
6400	$7.3309974\ 10^{-4}$	0.53343397	$4.4545754\ 10^{-4}$	0.49399631
12800	$5.1020991\ 10^{-4}$	0.52291857	$3.1266758\ 10^{-4}$	0.5106583

cells	total energy	rate
100	$7.6112265\ 10^{-4}$	–
200	$5.5497308\ 10^{-4}$	0.45571115
400	$4.6063172\ 10^{-4}$	0.26880405
800	$3.7798953\ 10^{-4}$	0.28526749
1600	$2.9584646\ 10^{-4}$	0.35349763
3200	$2.054455\ 10^{-4}$	0.52609289
6400	$1.4670834\ 10^{-4}$	0.48580482
12800	$1.0299897\ 10^{-5}$	0.51032105

The convergence rates are close to the expected values which prove convergence of the numerical solution to the exact solution.

5.4. Subsonic flow over a 2-D cylinder

The flow of a fluid over a 2-D cylinder is a typical benchmark case to test the behavior of a numerical method in the low Mach regime. For this test, an analytical solution is available in the incompressible limit or low Mach limit (REFS) and often referred to as potential flow. The main features of the potential flow are the following:

- The solution is symmetric: the iso-mach number lines are used to asses the symmetry of the numerical solution.
- The velocity at the top of the cylinder is twice the incoming velocity set at the inlet.
- The pressure fluctuations are proportional to the inlet Mach number square, as follows:

$$\tilde{P} = \frac{\max(P) - \min(P)}{\max(P)} \propto M_\infty^2$$

  where $\tilde{P}$ and M_∞ are the pressure fluctuations and the inlet Mach number, respectively.

The computational domain consists of a 1×1 square with a circular hole of radius 0.05 in its middle. At the inlet, a subsonic stagnation boundary condition is used: the stagnation pressure and temperature are computed using the following relations, valid for the Stiffened and Ideal gas equation of states:

$$\left\{ \begin{array}{l} P_0 = P\left(1+\frac{\gamma-1}{2}M^2\right)^{\frac{\gamma-1}{\gamma}} \\ T_0 = T\left(1+\frac{\gamma-1}{2}M^2\right) \end{array} \right. \tag{27}$$

The static pressure $P_s = 101325\ Pa$ is set at the subsonic outlet and a static pressure boundary type is used. The implementation of the pressure boundary conditions is done on the model of [19]. A solid wall boundary condition is set for the top and bottom walls of the computational domain: the normal velocity is zero since no mass can penetrate the sold body. The mesh is made of triangular cells.

The steady-state for Mach numbers ranging from $M_\infty = 10^{-3}$ to $M_\infty = 10^{-7}$ is shown in Fig. 5. The iso-Mach lines are drawn with 50 intervals ranging from 10^{-8} to M_∞, and allow to assess the symmetry of the numerical solution.

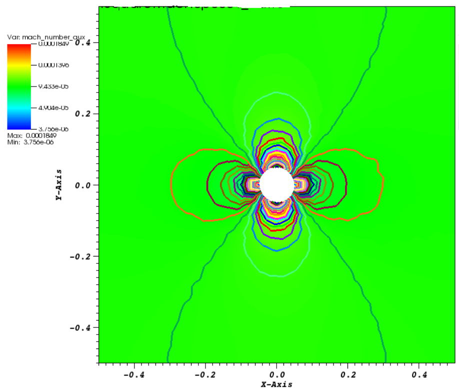

(a) Velocity solution at steady-state.

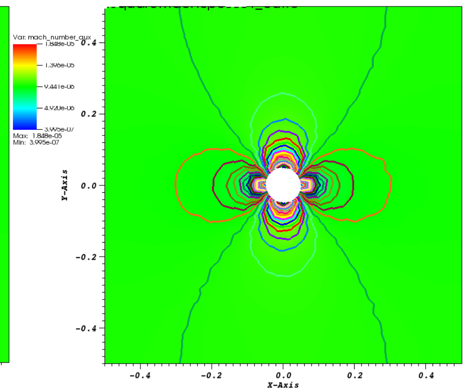

(b) Density solution at steady-state

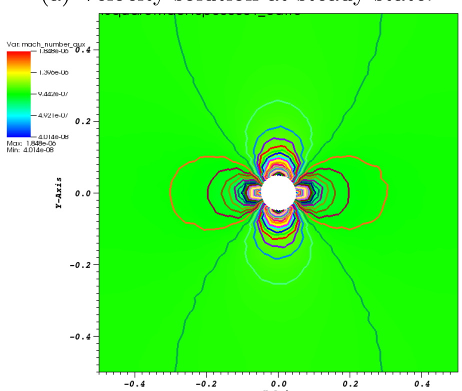

(c) Presolution at steady-state.

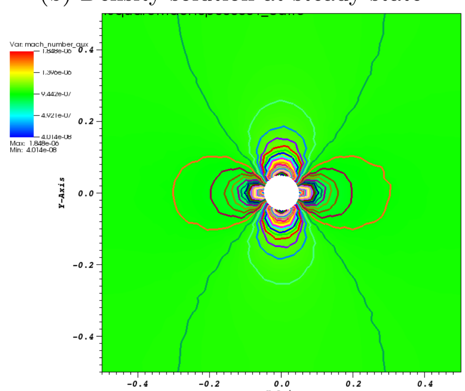

(d) Viscosity coefficients.

Figure 5: Steady-state solution for vapor phase in a 1-D convergent-divergent nozzle.

In Table 10, the velocity at the top of the cylinder and at the inlet are given for the different values of the Mach number presented in Fig. 5. The ratio of the inlet velocity to the velocity at the top of cylinder is also computed and is very close to 2 as expected.

Table 10: Velocity ratio for different Mach numbers.

Mach number	inlet velocity	velocity at the top of the cylinder	ratio
10^{-3}	$2.348\ 10^{-3}$	$1.176\ 10^{-3}$	1.99
10^{-4}	$2.285\ 10^{-4}$	$1.145\ 10^{-4}$	1.99
10^{-5}	$2.283\ 10^{-5}$	$1.144\ 10^{-5}$	1.99
10^{-6}	$2.283\ 10^{-6}$	$1.144\ 10^{-6}$	1.99
10^{-7}	$2.283\ 10^{-7}$	$1.144\ 10^{-7}$	1.99

5.5. Subsonic flow over a 2-D hump

This is a another example of an internal flow configuration. It consist of a channel of height $L = 1\ m$ and length $3L$, with a circular bump of length L and thickness $0.1L$. The bump is located on the bottom wall at a distance L from the inlet. The system is initialized with an uniform pressure $P = 101325\ Pa$ and temperature $T = 300\ K$. The initial velocity is computed from the Mach number, M, the pressure, the temperature and the Ideal Gas equation of state with the heat capacity $C_v = 717\ J/kg - K$ and the heat capacity ratio $\gamma = 1.4$. At the inlet, a subsonic stagnation boundary condition is used and the stagnation pressure and temperature are computed using Eq. (27). The static pressure $P_s = 101325\ Pa$ is set at the subsonic outlet. An uniform grid is used to get the numerical solution until steady-state is reached. The results are shown in Fig. 6a, Fig. 6b, Fig. 6c and Fig. 6d for the inlet Mach numbers $M = 0.7$, $M = 0.01$, $M = 10^{-4}$ and $M = 10^{-7}$, respectively. It is expected that, within the low Mach number range, the solution does not depend on the Mach number and is identical to the solution obtained with an incompressible flow code. On the other hand, for a flow at $M = 0.7$, the compressible effects become more important and shock can form.

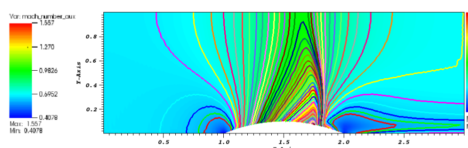

(a) Mach 0.7: iso-Mach lines at steady-state.

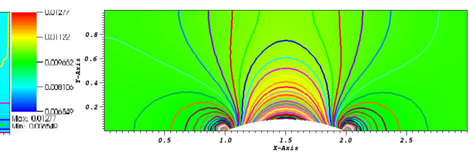

(b) Mach 10^{-2}: iso-Mach lines at steady-state.

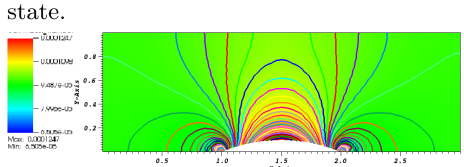

(c) Mach 10^{-5}: iso-Mach lines at steady-state.

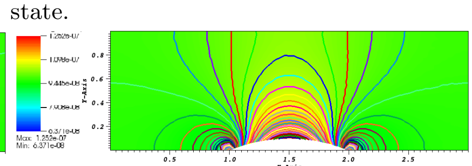

(d) Mach 10^{-7}: iso-Mach lines at steady-state.

Figure 6: Steady-state solution for a 2-D flow over a circular bump.

The results showed in Fig. 6b, Fig. 6c and Fig. 6d correspond to the low Mach regime. The iso-Mach lines are drawn ranging from the minimum and the maximum of each legend with 50 intervals. The steady-state solution is symmetric and does not depend on the value of the inlet Mach number as expected. In Fig. 6a, the steady-state numerical solution develops a shock: the compressibility effect are no longer negligible. The iso-Mach lines are also plotted with 50 intervals and ranging from 0.4 to 1.6. The shock is well resolved and does not display any instability or spurious oscillation.
The results presented in Fig. 6 were obtained with the new definition of the viscosity coefficient (see Eq. (21)), and, illustrate the capabilities of the entropy-

viscosity method to adapt to the type of flow (subsonic and transonic flows) without using any tuning parameters, but by just evaluating the entropy residual that is an indicator of the entropy production.

5.6. Supersonic flow in a compression corner

This is an example of a supersonic flow over a wedge of angle 15° where an oblique shock is generated at steady-state. The Mach number upstream of the shock is fixed to $M = 2.5$. The initial conditions are uniform: the pressure and temperature are set to $P = 101325\ Pa$ and $T = 300\ K$, respectively. The initial velocity is computed from the upstream Mach number and using the Ideal Gas equation of state with the same parameters as in Section 5.5. The code is run until steady-state. An analytical solution for this supersonic flow is available and give the downstream to upstream pressure, entropy and Mach number ratios [14]. The analytical and numerical ratios are given in see in Table 11.

Table 11: Analytical solution for the supersonic flow on an edge eat 15° at $M = 2.5$.

	analytical downstream to upstream ratio	numerical downstream to upstream ratio
Pressure	2.47	2.467
Mach number	0.74	0.741
Entropy	1.03	1.026

The inlet is supersonic and therefore, the pressure, temperature and velocity are specified using Dirichlet boundary conditions. The outlet is also supersonic and none of the characteristics enter the domain through this boundary: the values will be computed by the implicit solver.

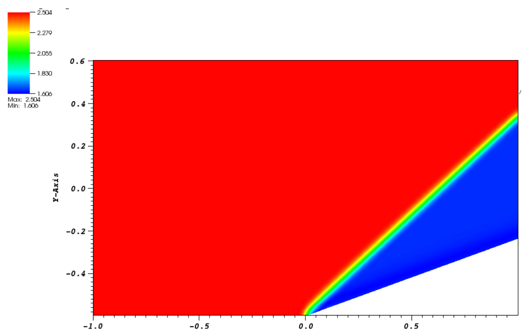

(a) Mach solution at steady-state.

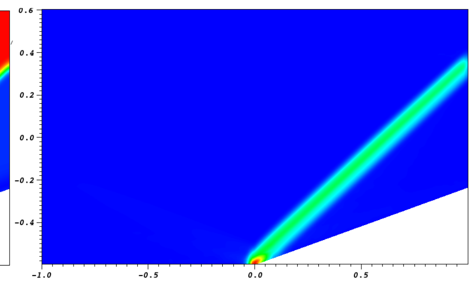

(b) Viscosity coefficient at steady-state.

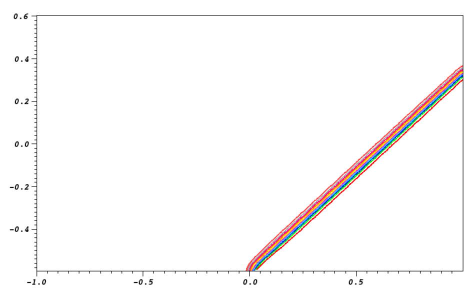

(c) Isomach at steady-state

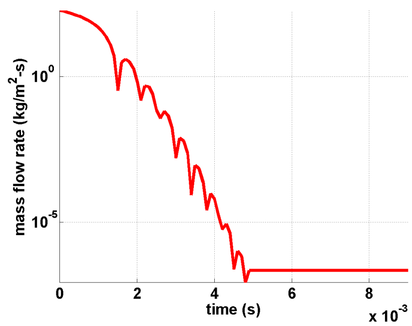

(d) Difference between inlet and outlet mass flow rates as a function of time.

Figure 7: Steady-state solution for a flow in a 2-D compression corner.

The steady-state numerical solution is given in Fig. 7: the Mach number, the viscosity coefficients are plotted in Fig. 7a and Fig. 7b, respectively. The steady-state solution is formed of two regions of constant states, separated by the oblique shock. In Fig. 7b, the viscosity coefficient is large in the shock, small anywhere else, and thus, behaves as expected. At the corner of the edge at $x = -0.25$ m, the viscosity coefficient is peaked because of the treatment of the wall boundary condition: at this particular node, the normal is not well defined and can cause numerical errors. The 1-D plots of the pressure and the mach number at $y = 0$, are also given in Fig. 7c: the shock does not show any spurious oscillations and is well resolved. Finally, the difference between the inlet and outlet mass flow rates is plotted in Fig. 7d and show that the steady-state is reached.

Overall, the numerical solution does not show any oscillations, match the analytical solution, and the shock is well resolved.

6. Conclusions

Acknowledgments

References

[1] J. L. Guermond, R. Pasquetti, Entropy viscosity method for nonlinear conservation laws, Journal of Comput. Phys 230 (2011) 4248–4267.

[2] J. L. Guermond, R. Pasquetti, Entropy viscosity method for high-order approximations of conservation laws, Lecture Notes in Computational Science and Engineering 76 (2011) 411–418.

[3] J. L. Guermond, B. Popov, Viscous regularization of the euler equations and entropy principles, under review.

[4] B. Cockburn, C. Johnson, C. Shu, E. Tadmor, Advanced numerical approximation of nonlinear hyperbolic equations, Lecture Notes in Mathematics 1697.

[5] B. Cockburn, G. Karniadakis, C. Shu, Discontinuous galerkin methods: theory, computation and applications, Lecture Notes in Computer Science and Engineering 11.

[6] R. Lohner, Applied CFD Techniques: an Introduction based on Finite Element Methods, 2^{nd} Edition Wiley, 2003.

[7] A. Lapidus, A detached shock calculation by second order finite differences, J. Comput. Phys. 2 (1967) 154–177.

[8] R. Lohner, K. Morgan, J. Peraire, A simple extension to multidimensional problems of the artificial viscosity due to lapidus, Commun. Numer. Methods Eng. 1(14) (1985) 141–147.

[9] J. Donea, A. Huerta, Finite Element Methods for Flow Problems, Oxford University Press, 2003.

[10] H. Guillard, C. Viozat, On the behavior of upwind schemes in the low mach number limit, Computers & Fluids 28 (1999) 63–86.

[11] E. Turkel, Preconditioned techniques in computational fluid dynamics, Annu. Rev. Fluid Mech. 31 (1999) 385–416.

[12] J. S. W. D. L, Darmofal, J. Peraire, The solution of the compressible euler equations at low mach numbers using a stabilized finite element algorithm, Comput. Methods Appl. Mech. Engrg. 190 (2001) 5719–5737.

[13] X.-S. Li, C.-W. Gu, An all-speed roe-type scheme and its asymptotic analysis of low mach number behavior, Journal of Computational Physics 227 (2008) 5144–5159.

[14] J. D. Anderson, Modern compressible flow, in: Guide for Verification and Validation in Computational Solid Mechanic., New York, 1982, pp. 10–2006.

[15] J. L. Guermond, R. Pasquetti, Entropy-based nonlinear viscosity for fourier approximations of conservation laws, in: C.R. Math. Acad. Sci., Vol. 326, Paris, 2008, pp. 801–806.

[16] V. Zingan, J. L. Guermond, J. Morel, B. Popov, Implementation of the entropy viscosity method with the discontinuous galerkin method, Journal of Comput. Phys 253 (2013) 479–490.

[17] B. Perthane, C. W. Shu, On positivity preserving finite volume schemes for euler equations, Numer. Math. 73 (1996) 119–130.

[18] E. F. Toro, Riemann Solvers and numerical methods for fluid dynamics, 2^{nd} Edition, Springer, 1999.

[19] R. Berry, R. Saurel, O. LeMetayer, The discrete equation method (dem) for fully compressible, two-phase flows in ducts of spatially varying cross-section, Nuclear Engineering and Design 240 (2010) 3797–3818.

[20] B. Muller, Low-mach number asymptotes of the navier-stokes equations, Journal of Engineering Mathematics 34 (1998) 97109.

[21] R. Loubere, Validation test case suite for compressible hydrodynamics computation, Theoritical Division T-7 Los Alamos National Laboratory.

[22] D. L. Darmofal, K. Siu, A robust multigrid algorithm for the euler equations with local preconditioning and semi-coarsening, Journal of Computational Physics 151 (1999) 728756.

[23] P. Perrot, A to Z of Thermodynamics, Oxford University Press, 1998.

[24] O. LeMetayer, J. Massoni, R. Saurel, Elaborating equation of state for a liquid and its vapor for two-phase flow models, International Journal of Thermal Science 43 (2004) 265–276.